RESOURCE

nature cell biology

Patchwork organization of the yeast plasma membrane into numerous coexisting domains

Felix Spira[1,3], Nikola S. Mueller[1,3], Gisela Beck[1], Philipp von Olshausen[2], Joachim Beig[1] and Roland Wedlich-Söldner[1,4]

The plasma membrane is made up of lipids and proteins, and serves as an active interface between the cell and its environment. Many plasma-membrane proteins are laterally segregated in the plane of the membrane, but the underlying mechanisms remain controversial. Here we investigate the distribution and dynamics of a representative set of plasma-membrane-associated proteins in yeast cells. These proteins were distributed non-homogeneously in patterns ranging from distinct patches to nearly continuous networks, and these patterns were in turn strongly influenced by the lipid composition of the plasma membrane. Most proteins segregated into distinct domains. However, proteins with similar or identical transmembrane sequences (TMSs) showed a marked tendency to co-localize. Indeed we could predictably relocate proteins by swapping their TMSs. Finally, we found that the domain association of plasma-membrane proteins has an impact on their function. Our results are consistent with self-organization of biological membranes into a patchwork of coexisting domains.

The plasma membrane is a highly specialized organelle that selectively mediates the import and export of a multitude of molecules, while serving as a platform for various signalling complexes. Efficient coordination of these functions is facilitated by lateral segregation of proteins into distinct domains[1,2]. However, most studies on membrane segregation have focused either on artificial membranes with relatively low complexity[3] or on selected protein classes, such as GPI-anchored proteins, in living cells[2]. Therefore, we do not know how prevalent lateral segregation of plasma-membrane components really is, and the mechanisms that drive lateral segregation of plasma-membrane components are still a matter of debate[3,4].

Several models have been advanced to explain the emergence of lateral heterogeneities in the distribution of proteins and lipids in membranes. The lipid-raft theory[4] postulates separation of liquid-ordered domains enriched in cholesterol and sphingolipids (rafts) from liquid-disordered domains mainly containing phospholipids. Protein–protein interactions[5], cortical actin[6] and the extracellular matrix[7] have also been proposed to influence plasma membrane organization. Since the formulation of the fluid-mosaic model of membranes, the authors of studies on artificial membranes have suggested mechanisms of self-organization that depend on weak interactions between multiple components[3,8]. According to these theories, lateral segregation should be considered an emergent property of all biological membranes.

In the plasma membrane of the budding yeast *Saccharomyces cerevisiae*, several amino-acid permeases, including the arginine permease Can1 cluster in the patch-like compartment MCC (membrane compartment occupied by Can1), whereas the membrane ATPase Pma1 occupies the network-like MCP (ref. 9). In addition, dynamic, patch-like domains were described for Tor Complex 2[1] and endocytic actin patches[10]. Other proteins were reported to be homogeneously distributed[9].

We have performed a large-scale characterization of plasma membrane organization in budding yeast by combining total internal reflection microscopy (TIRFM) with two-dimensional (2D) deconvolution. Our results indicate that biological membranes self-organize into patchworks of numerous coexisting domains.

RESULTS

Distribution patterns of plasma-membrane proteins

To systematically investigate lateral plasma membrane organization, we assembled a list of 279 proteins associated with the plasma membrane in *S. cerevisiae* (Supplementary Table S1). We further selected 46 representative proteins covering the main functional categories and types of membrane anchor (Fig. 1a and Supplementary Table S2). Lateral distribution and dynamics of each protein fused to GFP was then monitored in living cells by TIRFM. This technique minimizes out-of-focus excitation and is applicable to yeast cells,

[1]Cellular Dynamics and Cell Patterning, Max Planck Institute of Biochemistry, Am Klopferspitz 18, 82152 Martinsried, Germany. [2]Laboratory for Bio- and Nano-Photonics, Department of Microsystems Engineering-IMTEK, University of Freiburg, Freiburg 79110, Germany. [3]These authors contributed equally to this work. [4]Correspondence should be addressed to R.W.S. (e-mail: wedlich@biochem.mpg.de)

Received 10 January 2012; accepted 21 March 2012; published online 29 April 2012; DOI: 10.1038/ncb2487

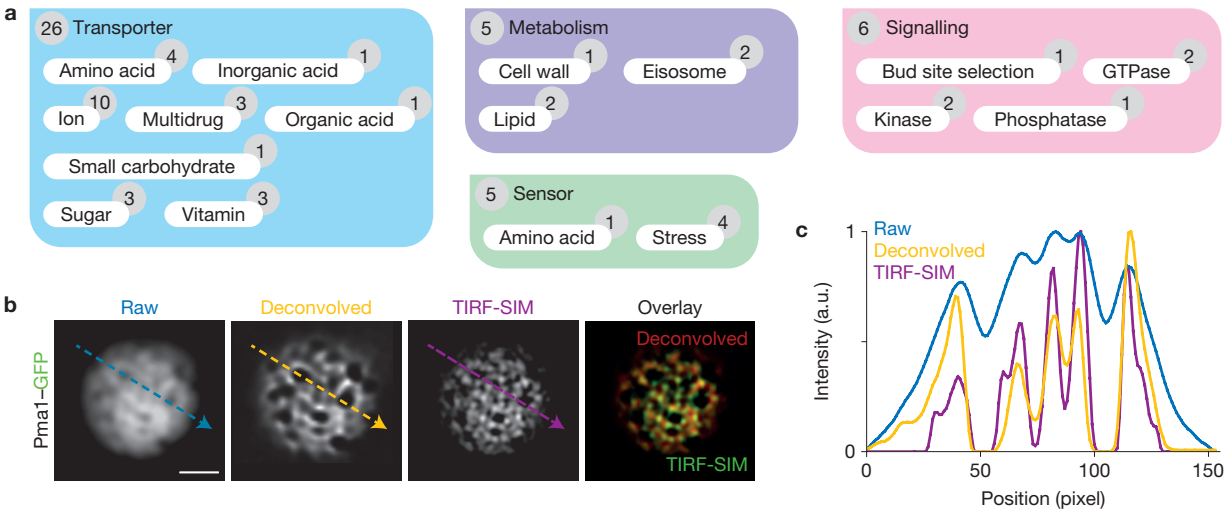

Figure 1 Test set of plasma-membrane proteins and imaging approach. (**a**) Schematic representation of the 46 plasma-membrane proteins chosen for analysis, and their functional categorization. The number of proteins in each category is indicated. Four proteins with unknown function are not shown. (**b**) Images of a Pma1–GFP-expressing cell seen by regular TIRFM (raw), TIRFM and deconvolution and TIRF-SIM. The overlay demonstrates the similarity of patterns observed by TIRF-SIM and deconvolution. Scale bar, 2 μm. (**c**) Intensity plots along the dashed arrows in **b**. Also see Supplementary Fig. S1 and Tables S1 and S2.

despite their thick cell walls[11]. Owing to turgor pressure, the yeast plasma membrane is largely flat, minimizing topological contributions to signal intensities in our images. Invaginations are found only at eisosomes[12] and actin patches[10].

By combining TIRFM with 2D deconvolution, we were able to visualize the distribution patterns of yeast plasma-membrane proteins with high contrast (Fig. 1b,c and Supplementary Fig. S1). Distribution patterns were already discernible in unprocessed TIRFM images and further enhanced by deconvolution (Fig. 1b,c and Supplementary Fig. S1, raw versus deconvolved). Images of uniformly distributed cytosolic proteins showed no discernible patterns after deconvolution (Supplementary Fig. S1a). In addition, patterns observed in deconvolved TIRFM images closely correspond to those obtained by TIRF structured illumination microscopy[13] (TIRF-SIM, Fig. 1b,c and Supplementary Fig. S1b). Hence, deconvolution does not remove or create any artefactual features in the original TIRFM images. The combination of TIRFM and deconvolution therefore provides a robust visualization method for the yeast plasma membrane.

All 46 proteins investigated were distributed non-homogeneously, forming patterns ranging from discrete patches to continuous networks (Fig. 2a,b and Supplementary Table S2). Most lipid-anchored proteins, as well as the lipid markers 2×(PH)-Plcδ for phosphatidylinositol-4,5-bisphosphate (PtdIns(4,5)P_2; ref. 14) and Lact-C2 for phosphatidylserine[15], formed network-like domains (Fig. 2a,c). We also found that Hxt1 and Gap1 (refs 1,16), two proteins previously reported to be homogeneously distributed, formed networks (Fig. 2d). To objectively characterize the range of observed patterns, we introduced a histogram-based parameter that we refer to as 'intensity distribution' (Supplementary Methods and Fig. S2a). This parameter yielded values close to 0 for patch-like patterns with large dark areas and up to 0.5 for network-like patterns with even distributions of grey values. Importantly, measured intensity distributions were characteristic for each protein (Fig. 2e and Supplementary Fig. S2b and Table S3).

To determine whether the intensity distribution merely reflected protein abundance, we quantified the fluorescence intensities of GFP-tagged proteins in the plasma membrane. Measured intensities covered three orders of magnitude (Supplementary Fig. S2c and Table S4) and were strongly correlated with previously determined protein expression levels[17] (Supplementary Fig. S2d). However, fluorescence intensities were only weakly correlated with intensity distributions ($R = 0.51$, Fig. 2f).

Taken together, our findings imply that most or all proteins in the yeast plasma membrane are distributed non-homogeneously into characteristic patterns that can be resolved by fluorescence microscopy.

Protein dynamics

The domains we observed were much larger than typical nanoclusters described for mammalian cells[18]. This may be attributable in part to the slow diffusion of lipids and plasma-membrane proteins in yeast[19,20]. To verify this, we analysed dynamics of our selected proteins by time-lapse TIRFM (Fig. 3a and Supplementary Movies S1–S4). Autocorrelation analyses showed that patterns of transmembrane plasma-membrane proteins remained constant or slowly reorganized over minutes (Fig. 3b). In contrast, lipid-anchored proteins (Ras2, Gpa1) and lipid markers (Lact-C2, 2×(PH)-Plcδ) rearranged within less than 1 s (Fig. 3a,b). In fluorescence recovery after photobleaching (FRAP) experiments, all transmembrane proteins exhibited very low diffusion rates ($t_{1/2} > 20$ s) and mobile fractions (<40% within 5 min, Supplementary Table S2). Rearrangement speeds were not correlated with intensity distributions or number of TMSs (Fig. 3c). With $t_{1/2}$ below 4 s (Fig. 3c) lipid-anchored proteins and lipid markers exhibited much higher mobility than integral plasma-membrane proteins, although diffusion of prenylated proteins and lipids in the yeast plasma membrane is still an order of magnitude slower than in mammalian cells[19,21].

In summary, integral yeast plasma-membrane proteins exhibit very slow lateral diffusion, whereas lipids and lipid-anchored proteins are much more mobile.

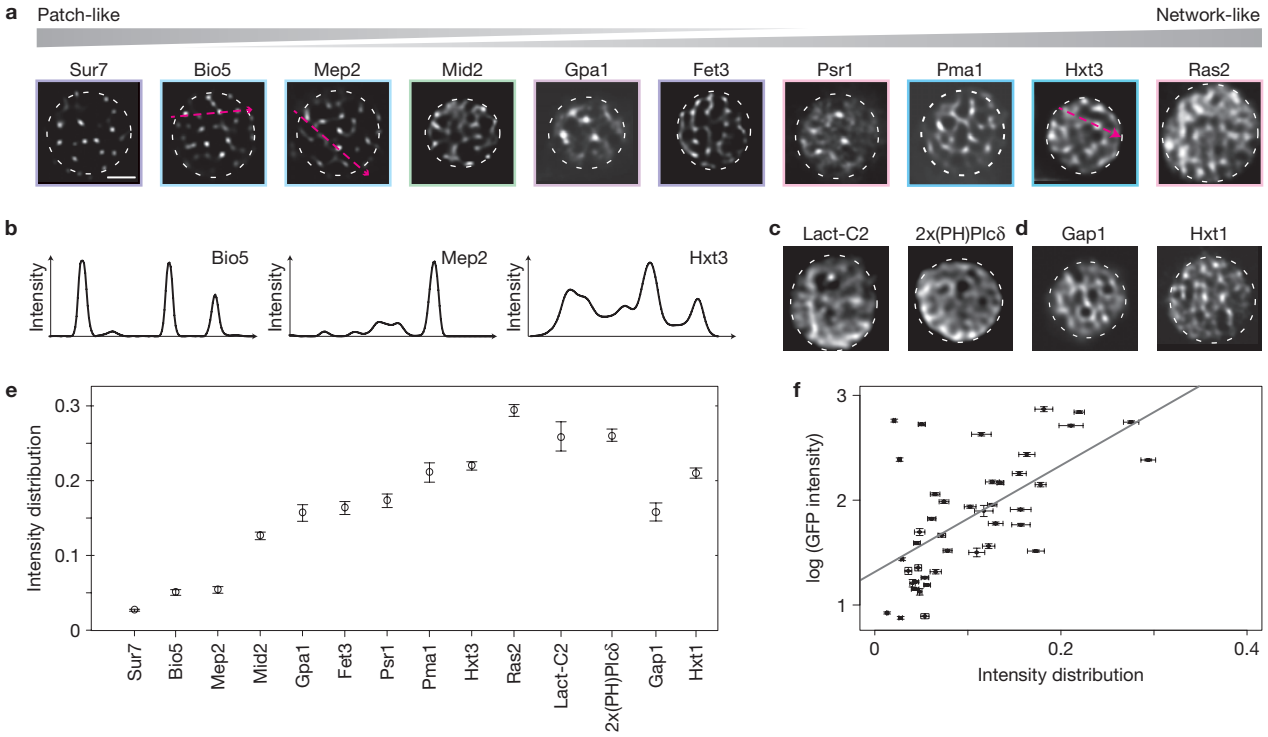

Figure 2 Localization patterns of plasma-membrane proteins. (**a**) TIRFM images of GFP-labelled proteins revealed inhomogeneous localization with patterns ranging from patch-like to network-like. Coloured frames represent functional classes as in Fig. 1a. (**b**) Representative intensity profiles of patch and network patterns along the dashed arrows in **a**. (**c**) Network distribution of lipid markers 2×(PH)-Plcδ (PtdIns(4,5)P_2) and Lact-C2 (phosphatidylserine). (**d**) Network patterns of two proteins previously reported to be homogeneously distributed. Scale bar, 2 μm. (**e**) Intensity distributions for proteins shown in **a**–**c** (data points: mean ± s.e.m.). See Methods for calculation of intensity distribution. (**f**) Weak correlation between intensity distribution and protein abundance of proteins in the test set. Abundance was estimated from GFP intensities at the cell periphery (data points: mean ± s.e.m.). See Supplementary Fig. S2 and Tables S2–S4 for **e**,**f** *n* and error bar values.

Coexistence of many protein domains

We next determined the degree of overlap between different plasma-membrane domains by imaging pairs of GFP- and RFP-tagged fusion proteins with two-colour TIRFM and channel-specific 2D deconvolution. To reliably analyse co-localization, we adjusted laser incidence angles for each channel and automated cell detection and image alignment (Supplementary Fig. S3a). We then used an intensity-based co-localization coefficient based on the Manders overlap[22] to assess the degree of co-localization (Supplementary Fig. S3b–d).

Initially, we quantified the degree of co-localization between proteins in our test set and the non-overlapping domains marked by Sur7 and Pma1 (refs 9,23). Co-localization values for these two proteins were used as positive and negative controls (Fig. 4a,e and Supplementary Fig. S4). With the exception of the known co-localizing protein Pil1 (refs 7,12), all tested proteins had low overlap values with patches formed by Sur7 (Fig. 4b,e and Supplementary Fig. S5a and Tables S2 and S6). The network-forming plasma membrane ATPase Pma1 co-localized to various degrees with proteins in our test set but never reached the high values of the positive controls (Fig. 4b,e and Supplementary Fig. S5b and Tables S2 and S6). Notably, some proteins with large intensity distribution values, such as Fet3, were clearly excluded from the Pma1 domain (Fig. 4b and Supplementary Movie S5), providing evidence against the existence of a single global network-like domain. We therefore extended our co-localization analysis to four additional proteins covering a range of intensity distributions. Again, the measured pair-wise overlap values (Fig. 4c,e and Supplementary Fig. S6a,b and Table S2) did not reach the values seen for identical proteins. To determine whether co-localization degree was related to sequence similarity, we measured pair-wise co-localization of four hexose transporters that are more than 66% identical in sequence. Indeed, all pairs showed high co-localization values (Fig. 4d,e and Supplementary Fig. S6c and Table S2).

In summary, our results indicate that integral plasma-membrane proteins localize to numerous coexisting domains that overlap only partially.

Random versus active protein segregation

To determine how proteins segregate into many coexisting domains, we needed to determine how much coincidental overlap was expected for particular pairs of domains. We therefore determined decoy overlap values by shuffling red and green channels from images of a particular strain and compared them with the actual co-localization results (Fig. 5a). We found that actual and decoy overlap values were highly correlated (Fig. 5b, $R = 0.89$, $P < 0.001$). For 70% of all pairs (88 of 125), co-localization values coincided with the expected random overlap (Fig. 5b, black). The others significantly deviated from their expected overlap values ($P < 0.05$) and included proteins that either actively co-localized (18, magenta), or excluded each other (19, cyan; Fig. 5b and Supplementary Fig. S7a and Table S6). Notably, proteins with identical or similar sequences co-localized to a greater degree than expected by chance. In contrast, the Sur7 domain excluded a large

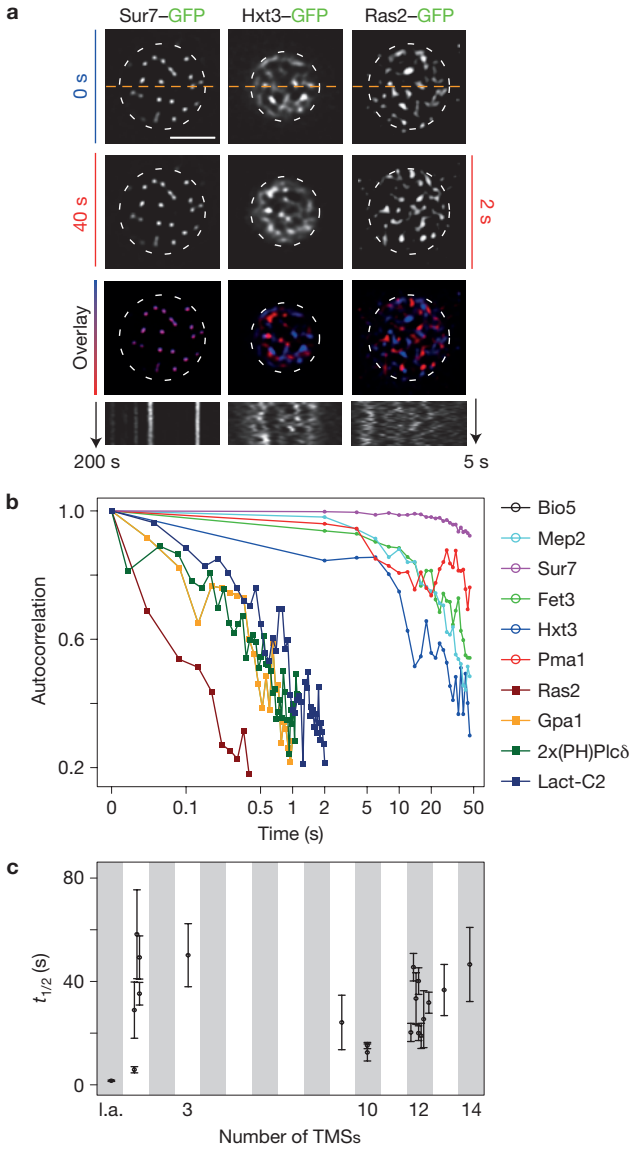

Figure 3 Dynamics of plasma-membrane proteins. (**a**) Representation of protein movement by overlay of images taken 40 s (Sur7, Hxt3) or 2 s (Ras2) apart. Kymographs were taken along the indicated dashed lines. Scale bar, 2 μm. (**b**) Autocorrelation curves for GFP signals of proteins shown in Fig. 1. Time is plotted on a logarithmic scale to represent the different timescales of reorganization. Also see Supplementary Movies S1–S4. (**c**) FRAP half-times of plasma-membrane protein shown as a function of the number of TMS segments (data points: mean ± s.e.m.). See Supplementary Table S2 for *n* values. l.a., lipid anchored.

number of plasma-membrane proteins (Supplementary Table S6). Several of the significantly overlapping domains such as Sur7–Pil1, Pma1–Nha1 or Hxt3–Hnm1 have been functionally linked before[12,24,25], whereas the significance of other overlaps (for example, Pma1–Yor1 and Pma1–Mrh1) has yet to be determined.

We next wanted to identify parameters affecting domain overlap. We found highly significant correlation between co-localization and joint intensity distributions (Fig. 5c, $R = 0.71$, $P < 0.001$) but only weak correlation with protein abundance (Supplementary Fig. S7b). To investigate the influence of intensity distribution on protein co-localization in more detail, we generated decoy values using images from different strains but with similar intensity distributions. We then gradually increased the divergence between the reference intensity distributions and those used for decoy calculations. As expected, correlation between decoy and actual overlap values declined rapidly with increasing divergence in intensity distributions (Fig. 5d and Supplementary Fig. S7c).

In summary, correlation analyses clearly demonstrated that the intensity distribution of a particular protein, reflecting its spatial pattern, has a strong influence on its co-localization with other proteins.

Factors affecting plasma-membrane pattern formation

We next wanted to determine the cause for clustering of plasma-membrane proteins in characteristic patterns. Previously proposed mechanisms for lateral protein segregation invoke association with the extracellular matrix[7] or cortical actin cytoskeleton[6]. The factor most often implicated in driving protein segregation in membranes is lipid composition[4]. We examined each of these options by measuring effects on intensity distributions.

Enzymatic degradation of the cell wall led to marked changes in plasma-membrane protein patterns and frequent aggregation of proteins into large patches (Supplementary Fig. S8a). Depolymerization of the actin cytoskeleton by exposure to latrunculin B had only minor effects on intensity distributions (Fig. 6a, LatB), consistent with the fast reorganization of actin when compared with integral plasma-membrane protein diffusion[10,11]. This indicates that actin-dependent endocytosis and secretion play only minor roles in the maintenance of segregation patterns.

We used several approaches to perturb the lipid composition of the plasma-membrane. The drug myriocin inhibits sphingosine biosynthesis and depletes sphingolipids[26]. Deletion of *cho1* blocks the canonical pathway of phospholipid synthesis. In medium supplemented with choline, this leads to a selective reduction of phosphatidylserine levels[27], as confirmed by Lact-C2 localization (Supplementary Fig. S8b). Sterol composition is strongly altered in Δ*erg3*Δ*erg6* cells[28]. Finally, a temperature-sensitive allele of the phosphatidylinositol kinase *mss4-102* (ref. 29) allows reduction of PtdIns(4,5)P_2 levels.

All lipid perturbations had strong effects on intensity distributions but differed in their target range (Fig. 6a and Supplementary Table S9). Nearly all changes increased values of intensity distribution; that is, reduction in lipid complexity is associated with reduced protein segregation. Whereas depletion of sphingolipids (myriocin) and reduced PtdIns(4,5)P_2 levels affected only a subset of proteins, removal of *cho1* or modification of sterol composition affected the intensity distributions of all markers investigated (Fig. 6a).

To determine whether the observed effects of *cho1* deletion were indeed due to depletion of phosphatidylserine, we supplemented Δ*cho1* cells with lyso-phosphatidylserine. Successful incorporation of phosphatidylserine into the plasma membrane was monitored with GFP–Lact-C2 (Supplementary Fig S8b). Remarkably, within 1 h after lyso-phosphatidylserine addition, intensity distributions for some proteins, such as Bio5, were restored to wild-type levels (Fig. 6b,c). Lack of, or incomplete, recovery of other investigated proteins could be due to long-lasting defects in membrane transport in Δ*cho1* cells. Indeed, after growth in lyso-phosphatidylserine overnight, the intensity distribution of Pmp1 had returned to wild-type levels (Fig. 6c). Our results thus indicate that lipid composition differentially influences lateral protein segregation in the yeast plasma membrane.

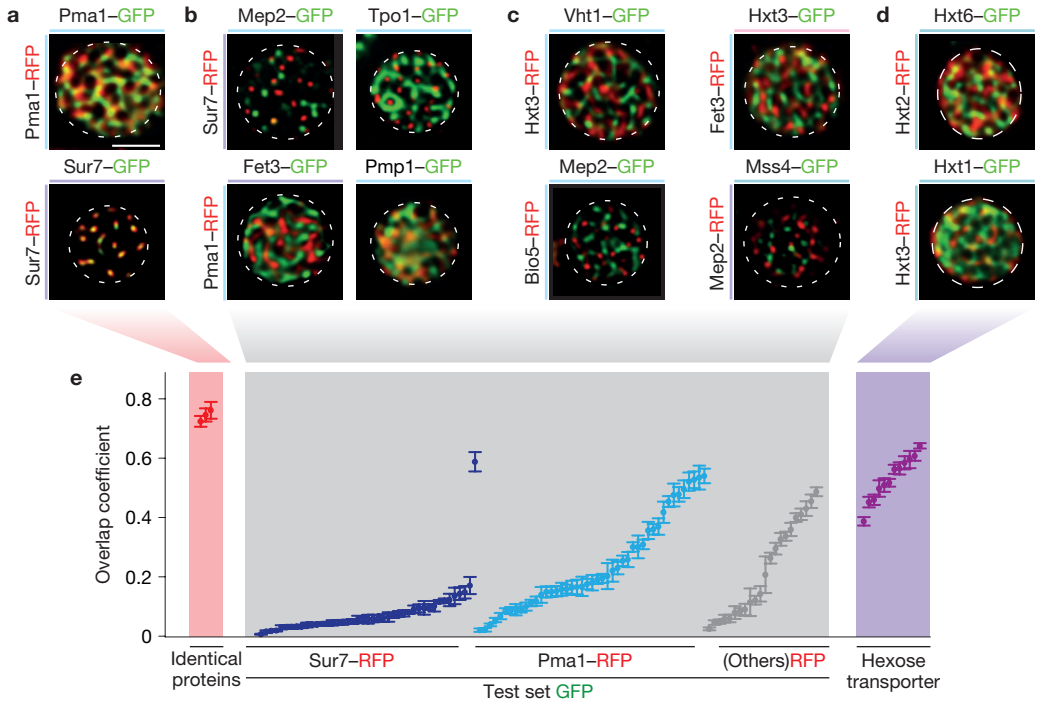

Figure 4 Coexistence of multiple plasma-membrane protein domains. (**a**–**d**) Two-colour TIRFM images of strains expressing plasma-membrane proteins labelled with GFP and RFP: examples of co-localization for RFP- and GFP-labelled versions of the same protein (**a**), the known domain markers Sur7 and Pma1 (**b**), further proteins with varying intensity distributions (**c**) and different hexose transporters (**d**) Scale bar, 2 μm. (**e**) Overlap coefficients for all examined protein pairs. Overlap values are shown as box plots (data points: mean ± s.e.m.; see Methods for details). Also see Supplementary Figs S3–S6, Table S5 for *n* values (**e**) and Supplementary Movie S5.

The role of transmembrane regions

Lipid–protein interactions are expected to occur largely through TMSs or lipid anchors. To determine whether TMSs contribute to protein segregation, we determined the degree of overlap between the single TMS of Pmp1 and the full-length protein. Remarkably, the TMS of Pmp1 significantly co-localized with full-length Pmp1 (Fig. 7a,d). The TMSs of Mid2 and Fet3 also co-localized with Pmp1, albeit to lesser extents, reflecting their lower degrees of sequences similarity (Fig. 7a, Finally, full-length Fet3 showed random overlap with Pmp1 (Fig. 7b,d), consistent with its low sequence similarity in the range of randomly generated TMSs (Supplementary Fig. S8c). Importantly, differences in co-localization levels did not result from variations in decoy correlation or intensity distributions (Fig. 7c,d). These results indicate that TMSs of proteins contribute directly to lateral segregation.

To determine whether TMSs could direct entire proteins to particular domains, we expressed a chimaera between Fet3 and the TMS of Pmp1 (FetPmp). The monomeric Fet3 significantly co-localized with itself but only randomly with Pmp1 (Fig. 8a). In contrast, the FetPmp chimaera showed random overlap with Fet3, but co-localized significantly with Pmp1 (Fig. 8a). Therefore, a TMS of 22 amino acids was sufficient to redirect a 600-amino-acid protein to a different plasma-membrane domain.

Functional relevance of plasma-membrane domains

The FetPmp chimaera also provided a tool for studying the functional relevance of domain formation. The ferro-O_2-oxireductase Fet3 is essential for growth in low-iron media (Supplementary Fig. S8d). The growth defect of Δ*fet3* cells could be rescued by wild-type Fet3 but not by the FetPmp chimaera (Supplementary Fig. S8d). Hence, the TMS swap not only effectively segregated the FetPmp chimaera into the Pmp1 domain but also impaired iron uptake. At this stage, we cannot rule out the possibility that swapping TMSs affects the enzymatic activity of Fet3. We therefore further examined the functional relevance of membrane domains by mis-localizing Can1, which is significantly enriched in the immobile MCC domain (Supplementary Fig. S8e,f and Table S6). Wild-type yeast cells are sensitive to the toxic arginine analogue canavanine, which is taken up by Can1 (ref. 30). Resistance to canavanine was therefore used to monitor function of Can1. To alter Can1 localization, we used GFP-binder (GB), a monomeric, high-affinity GFP antibody[31]. When we co-expressed Pma1–GB and Can1–GFP, Can1–GFP was displaced from MCC patches[9] marked by Sur7–RFP (Fig. 8b and Supplementary Fig. S8e,f and Table S6). Importantly, cells expressing displaced Can1 were able to grow on canavanine-containing medium, comparable to Δ*can1* cells (Fig. 8c).

To assess whether Can1 function specifically requires MCC association, we performed several control experiments. Using the GFP-binder to tether Can1 to Sur7 (ref. 23), another MCC resident, efficiently retained Can1 in its domain and had no effect on Can1 function (Fig. 8c), providing evidence against unspecific effects of the GFP-binder. We also disrupted Can1 localization by either deleting the eisosomal core component *PIL1* (ref. 32), or the regulatory factor *NCE102*, which affects the number of eisosomes[33] and is important for recruitment of Can1 to the MCC domain[16]. On deletion of *PIL1*, MCC domains marked by Sur7–RFP collapsed to remnants, which still weakly co-localized with Can1–GFP (Supplementary Fig. S8e, arrowheads). On low canavanine concentrations, Δ*pil1* cells exhibited moderate growth (Fig. 8c), indi-

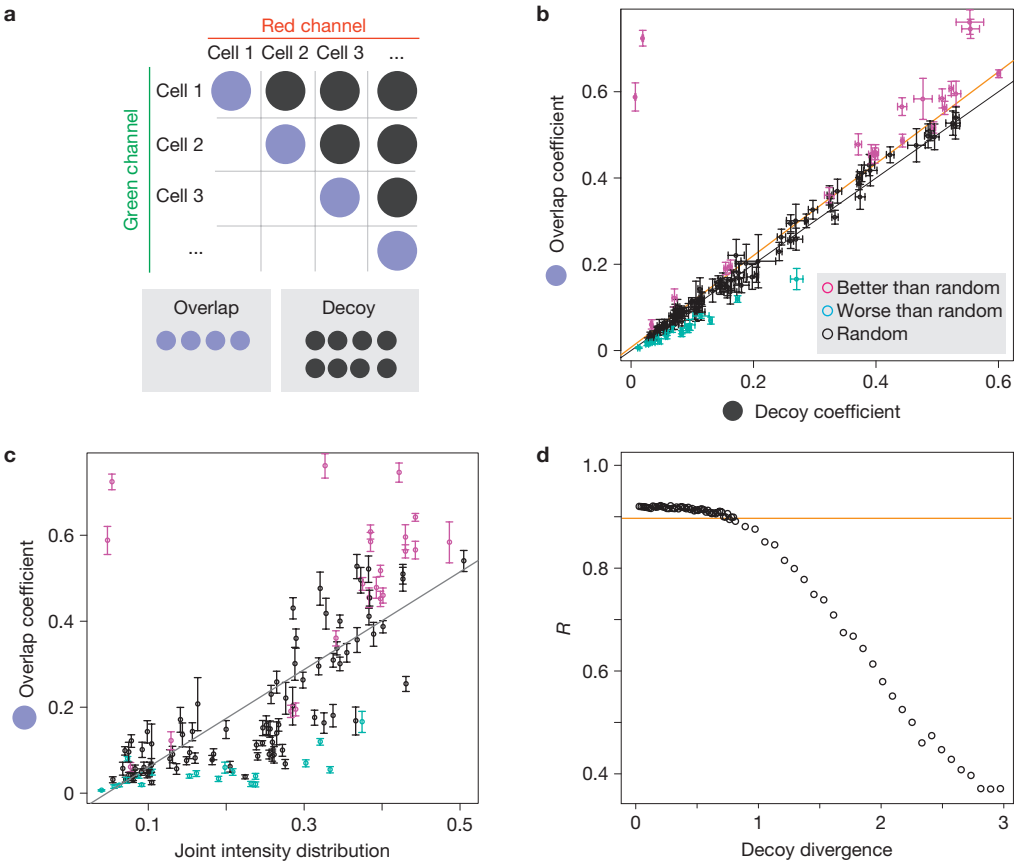

Figure 5 Real and random overlap value. (**a**) Schematic representation of selection procedure for calculation of real (red and green channels from the same cell) and decoy (red and green channels from different cells of the same strain) overlap values. (**b**) Correlation between real and decoy overlap coefficients (termed overlap coefficient and decoy coefficient, respectively). The values were highly correlated with a Pearson coefficient of $R = 0.89$ (orange line, $P < 0.001$). Data points are shown as mean ± s.e.m. in both directions. The black line indicates identity. Protein pairs co-localizing significantly ($P < 0.05$) better or worse than expected from decoy values are shown in magenta and cyan, respectively. (**c**) Correlation between overlap coefficient and joint intensity distribution (sum of intensity distributions). (Data points: mean ± s.e.m.). $R = 0.71$, $P < 0.001$, grey line. Colour code as in **b**. $n > 20$ for decoy values (**b**). See Supplementary Table S5 for n values of overlap coefficients (**b**,**c**). (**d**) Calculation of decoy values using cells with defined intensity distributions. The correlation (R) between decoy and real overlap values is lost with increasing divergence between intensity distributions of the original images and those of the selected decoy cells. Divergence is plotted as a z score. Also see Supplementary Fig. S7 and Table S6.

cating reduced Can1 functionality. On deletion of *NCE102*, consistent with a previous report[16], enrichment of Can1–GFP in MCC patches was clearly reduced when compared with wild-type cells (Supplementary Fig. S8e,f and Table S6) and Can1–GFP exhibited an increased intensity distribution (Supplementary Fig. S8g). However, Can1 still significantly co-localized with Sur7 (Supplementary Fig. S8e,f and Table S6) and this residual association of Can1 with MCC in Δ*nce102* cells was consistent with Can1 functionality and hence absence of canavanine resistance (Fig. 8c). Finally, reduced or increased Can1–GFP levels in deletion strains or strains co-expressing GFP-binder fusions, respectively, did not correlate with resistance to canavanine (Fig. 8c and Supplementary Fig. S8h). Under our experimental conditions, Can1 was generally not detectable on internal membranes (Supplementary Fig. S8i). In summary, our results indicate that association of Can1 with the MCC domain is important for its proper biological function.

DISCUSSION

Our findings indicate that proteins in biological membranes self-organize into numerous partially overlapping domains. In this 'patchwork' membrane, protein domains randomly overlap with each other depending on their sizes and shapes.

Our study of lateral protein segregation was facilitated by the unusually large size and temporal stability of domains formed in the yeast plasma membrane. This type of organization has typically not been seen in mammalian cells, where domains are mostly short-lived and too small to be resolved by conventional light microscopy[2]. This is one reason why the mechanisms controlling lateral segregation have been so difficult to address. The yeast plasma membrane therefore constitutes an attractive model system for the elucidation of fundamental principles contributing to the organization of biological membranes.

Patchiness of membranes was previously suggested[3,34] and is thought to reflect segregation of membrane components by weak protein–lipid interactions. As every protein may simultaneously interact with different lipids and vice versa, the number of putative combinations between cellular lipid species[35] and transmembrane proteins[36] can easily accommodate the large number of patterns observed in this study (Fig. 2). A combinatorial model of protein–lipid interactions was recently proposed for lipid-binding proteins[37], supporting a

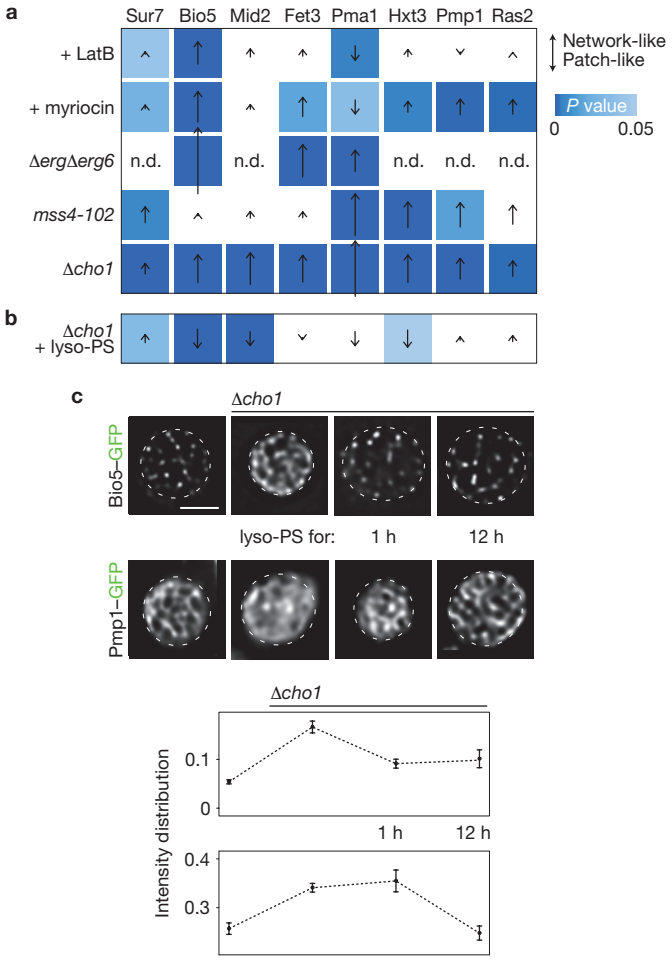

Figure 6 Changing localization patterns of plasma-membrane proteins. (**a**) Matrix showing the effects of perturbations of the actin cytoskeleton (LatB) or lipid composition on intensity distributions of selected proteins. Arrows indicate the direction and extent of change when compared with control cells. Colours indicate level of significance with white being not significant. n.d., not determined, strain could not be generated. (**b**) Reversibility of Δ*cho1* effects on intensity distributions after supplementing media with (lyso-PS). Distribution of some proteins (for example, Bio5) reverts back to control patterns. (**c**) Distribution patterns of Pmp1–GFP and Bio5–GFP in Δ*cho1* strains supplemented with lyso-phosphatidylserine for different time periods (data points: mean ± s.e.m.). Bio5–GFP intensity distributions already recovered after 1 h, whereas Pmp1 was affected only after 12 h. Scale bar, 2 μm. See Supplementary Fig. S8a,b and Table S9 for *n* values (**a**,**c**) except at 12 h timepoint (**c**), for which $n = 5$ (upper panel) and $n = 6$ (lower panel).

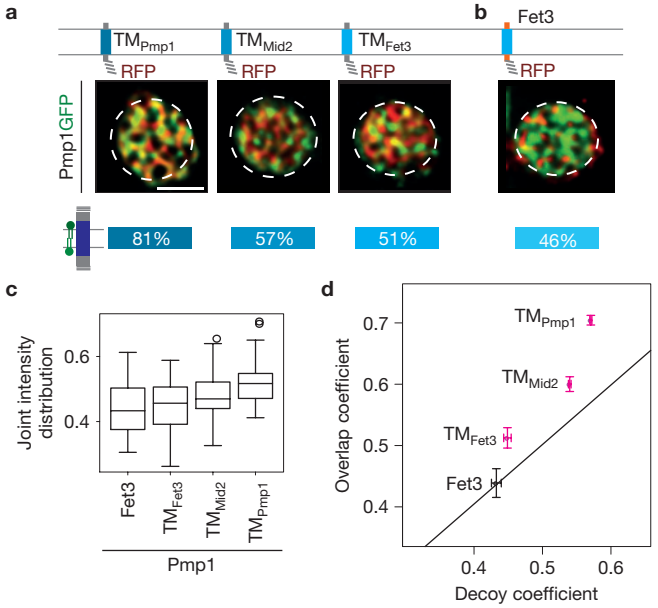

Figure 7 Influence of TMSs on protein localization. (**a**) Localization patterns of synthetic TMS–RFP fusion constructs. TMSs of the single-spanning transmembrane (TM) proteins Pmp1, Mid2 and Fet3 were co-localized with full-length Pmp1–GFP. Sequence identities between TMS regions are indicated as a percentage. Scale bar, 2 μm. (**b**) Co-localization and TMS sequence identity between Fet3 and Pmp1. (**c**) Similar joint intensity distributions for protein pairs in **a** and **b**. Circles represent outliers; see Methods for details. (**d**) Correlation between real and decoy overlap values for indicated TMS constructs with Pmp1 (data points: mean ± s.e.m.). All pairs with sequence identity above random values significantly co-localized (random overlap: black line, magenta: increased overlap, $P < 0.05$), whereas Fet3 and Pmp1 had random TMS similarity (Supplementary Fig. S8c) and also co-localized at random levels. See Supplementary Table S5 for *n* values (**c**,**d**).

mechanism for the interpretation of patchwork membrane domains by signalling molecules.

The patchwork membrane combines features of several membrane models. Interfacial or annular lipids have been proposed to match the membrane proteins they encompass[3]. This matching could occur through selection of lipid chain lengths[36], through fitting of lipids into the shapes dictated by membrane proteins[38] or by matching of charges[39]. A significant role for lipid charges is indicated by strong effects of phosphatidylserine perturbations on domain patterns (Fig. 6), with phosphatidylserine constituting a large portion of the inner plasma-membrane leaflet[15]. In addition, our co-localization results point to a role for the TMSs in domain selection, in line with studies where local mutations in TMS sequences were sufficient to alter domain association of proteins[40].

Although our proposed mechanism of membrane self-organization is intuitively appealing, it is not immediately obvious how it can lead to formation of the characteristic large-scale patterns in the yeast plasma membrane. One important factor is certainly the unusually slow diffusion of integral membrane proteins[19] (Fig. 2). This would also explain why comparable domains have not been observed in mammalian systems, where membrane proteins and lipids diffuse at much faster rates[20,41]. One consequence of faster lipid diffusion would be shorter coherence lengths, and hence smaller domains. Such correlations between domain size and protein/lipid dynamics were predicted by theoretical approaches[42], and reported for lipid rafts, which can form macroscopic domains in budding yeast[43] but much smaller and more dynamic nanoclusters in mammalian cells[18]. An extension of our findings would postulate the existence of many different nanometre-sized protein domains in higher eukaryotes, with classical rafts as one particular case. Indeed, two mutually exclusive sphingolipid-containing domains were recently identified in mammalian cells[44].

Self-organization of biological membranes through lipid–protein interactions provides a basis on which additional mechanisms for lateral segregation can build. Protein–protein[5] and protein–cell-wall interactions[7], as well as cytoskeletal fences[6], have been shown to support lateral segregation of specific components. Although actin in yeast

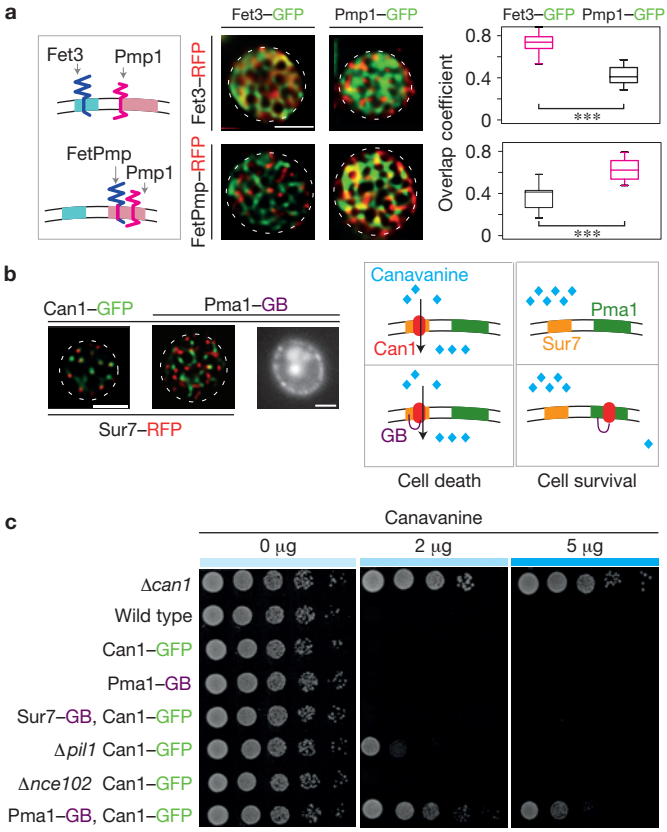

Figure 8 Artificial re-targeting of plasma-membrane proteins. (**a**) Schematic representation and co-localization of FetPmp, a chimaeric construct, in which the Fet3 TMS is replaced by the Pmp1 TMS. This results in the relocation of Fet3Pmp to the Pmp1 domain. Box plots show overlap coefficients. $^{***}P < 0.01$. See Supplementary Table S5 for *n* values. (**b**) Two-colour TIRFM images and schematic representation showing the displacement of Can1–GFP from its native domain (marked by Sur7) by co-expression of a Pma1–GB fusion. The equatorial image shows that Can1–GFP does not become internalized after addition of canavanine. Scale bar, 2 μm. (**c**) Growth assays with and without canavanine. Ectopic relocalization of Can1 to the Pma1 domain by Pma1–GB as well as removal of eisosomes (Δ*pil1*) results in loss or reduction of Can1 function, as indicated by resistance to canavanine. Retention in patches by binding to Sur7–GB or reduction of Can1 recruitment to MCC by deletion of *NCE102* does not noticeably affect Can1 function. Also see Supplementary Fig. S8d–i.

reorganizes faster than most integral plasma-membrane proteins[11] and plays a minor role in protein segregation (Fig. 6a), we have found large changes in domain patterns on cell wall degradation (Supplementary Fig. S8a). However, cell wall removal presumably has many indirect effects on actin organization and plasma membrane composition[11], making our results difficult to interpret. In addition, it is difficult to imagine how the isotropic and static cell wall could give rise to a large number of distinct protein domains.

The importance of correct domain association has been shown for various raft-associated proteins as well as for amino-acid permeases in yeast[45]. Can1 is known to require ergosterol for its function and plasma membrane targeting[9,46]. The MCC domain, which has been reported to be enriched in ergosterol[16], might therefore constitute a specific lipid environment that promotes Can1 function. Ultimately, we expect that a patchwork organization of membranes promotes the cell's ability to perform a large variety of tightly regulated biological functions in highly crowded environments. □

METHODS

Methods and any associated references are available in the online version of the paper at www.nature.com/naturecellbiology

Note: Supplementary Information is available on the Nature Cell Biology website

ACKNOWLEDGEMENTS

We are indebted to A. Rohrbach for providing access to the TIRF-SIM microscope and analysis. We thank N. Johnsson (Institute for Molecular Genetics and Cell Biology, Ulm University, Germany) for providing the plasmid ACP–Sag1 and P. Hardy for editorial assistance. This work was financially supported by the Max Planck Society.

AUTHOR CONTRIBUTIONS

R.W-S., F.S. and N.S.M. designed all experiments. F.S. performed all microscopy and experiments with help from G.B. N.S.M., F.S., J.B. and R.W-S. analysed the data. P.v.O. and F.S. performed the TIRF-SIM experiments. F.S., N.S.M. and R.W-S. wrote the paper.

COMPETING FINANCIAL INTERESTS

The authors declare no competing financial interests.

Published online at www.nature.com/naturecellbiology
Reprints and permissions information is available online at www.nature.com/reprints

1. Berchtold, D. & Walther, T. C. TORC2 plasma membrane localization is essential for cell viability and restricted to a distinct domain. *Mol. Biol. Cell* **20,** 1565–1575 (2009).
2. Sharma, P. *et al.* Nanoscale organization of multiple GPI-anchored proteins in living cell membranes. *Cell* **116,** 577–589 (2004).
3. Bagatolli, L. A., Ipsen, J. H., Simonsen, A. C. & Mouritsen, O. G. An outlook on organization of lipids in membranes: searching for a realistic connection with the organization of biological membranes. *Prog Lipid Res.* **49,** 378–389 (2010).
4. Lingwood, D., Kaiser, H. J., Levental, I. & Simons, K. Lipid rafts as functional heterogeneity in cell membranes. *Biochem. Soc. Trans.* **37,** 955–960 (2009).
5. Douglass, A. D. & Vale, R. D. Single-molecule microscopy reveals plasma membrane microdomains created by protein–protein networks that exclude or trap signaling molecules in T cells. *Cell* **121,** 937–950 (2005).
6. Kusumi, A., Sako, Y. & Yamamoto, M. Confined lateral diffusion of membrane receptors as studied by single particle tracking (nanovid microscopy). Effects of calcium-induced differentiation in cultured epithelial cells. *Biophys. J.* **65,** 2021–2040 (1993).
7. Sackmann, E., Lipowsky, R. & Sackmann, E. *Handbook of Biological Physics* Vol. 1, Part 1, 1–63 (North-Holland, 1995).
8. Anderson, R. G. & Jacobson, K. A role for lipid shells in targeting proteins to caveolae, rafts, and other lipid domains. *Science* **296,** 1821–1825 (2002).
9. Malínská, K., Malínská, J., Opekarová, M. & Tanner, W. Visualization of protein compartmentation within the plasma membrane of living yeast cells. *Mol. Biol. Cell* **14,** 4427–4436 (2003).
10. Kaksonen, M., Toret, C. P. & Drubin, D. G. A modular design for the clathrin- and actin-mediated endocytosis machinery. *Cell* **123,** 305–320 (2005).
11. Yu, J. H., Crevenna, A. H., Bettenbuhl, M., Freisinger, T. & Wedlich-Soldner, R. Cortical actin dynamics driven by formins and myosin V. *J. Cell Sci.* **124,** 1533–1541 (2011).
12. Walther, T. C. *et al.* Eisosomes mark static sites of endocytosis. *Nature* **439,** 998–1003 (2006).
13. Fiolka, R., Beck, M. & Stemmer, A. Structured illumination in total internal reflection fluorescence microscopy using a spatial light modulator. *Opt. Lett.* **33,** 1629–1631 (2008).
14. Stauffer, T. P., Ahn, S. & Meyer, T. Receptor-induced transient reduction in plasma membrane PtdIns(4,5)P2 concentration monitored in living cells. *Curr. Biol.* **8,** 343–346 (1998).
15. Yeung, T. *et al.* Membrane phosphatidylserine regulates surface charge and protein localization. *Science* **319,** 210–213 (2008).
16. Grossmann, G. *et al.* Plasma membrane microdomains regulate turnover of transport proteins in yeast. *J. Cell Biol.* **183,** 1075–1088 (2008).
17. Ghaemmaghami, S. *et al.* Global analysis of protein expression in yeast. *Nature* **425,** 737–741 (2003).
18. Goswami, D. *et al.* Nanoclusters of GPI-anchored proteins are formed by cortical actin-driven activity. *Cell* **135,** 1085–1097 (2008).
19. Greenberg, M. L. & Axelrod, D. Anomalously slow mobility of fluorescent lipid probes in the plasma membrane of the yeast *Saccharomyces cerevisiae*. *J. Membr. Biol.* **131,** 115–127 (1993).
20. Valdez-Taubas, J. & Pelham, H. R. B. Slow diffusion of proteins in the yeast plasma membrane allows polarity to be maintained by endocytic cycling. *Curr. Biol.* **13,** 1636–1640 (2003).

21. Marco, E., Wedlich-Soldner, R., Li, R., Altschuler, S. J. & Wu, L. F. Endocytosis optimizes the dynamic localization of membrane proteins that regulate cortical polarity. *Cell* **129,** 411–422 (2007).
22. Manders, E. M. M., Verbeek, F. J. & Aten, J. A. Measurement of co-localization of object in dual-colour confocal images. *J. Microsc.* **169,** 375–382 (1993).
23. Malinska, K., Malinsky, J., Opekarova, M. & Tanner, W. Distribution of Can1p into stable domains reflects lateral protein segregation within the plasma membrane of living *S. cerevisiae* cells. *J. Cell Sci.* **117,** 6031–6041 (2004).
24. Flegelova, H. & Sychrova, H. Mammalian NHE2 Na(+)/H+ exchanger mediates efflux of potassium upon heterologous expression in yeast. *FEBS Lett.* **579,** 4733–4738 (2005).
25. Tarassov, K. *et al.* An *in vivo* map of the yeast protein interactome. *Science* **320,** 1465–1470 (2008).
26. Momoi, M. *et al.* SLI1 (YGR212W) is a major gene conferring resistance to the sphingolipid biosynthesis inhibitor ISP-1, and encodes an ISP-1 *N*-acetyltransferase in yeast. *Biochem. J.* **381,** 321–328 (2004).
27. Hikiji, T., Miura, K., Kiyono, K., Shibuya, I. & Ohta, A. Disruption of the CHO1 gene encoding phosphatidylserine synthase in *Saccharomyces cerevisiae*. *J. Biochem.* **104,** 894–900 (1988).
28. Heese-Peck, A. *et al.* Multiple functions of sterols in yeast endocytosis. *Mol. Biol. Cell* **13,** 2664–2680 (2002).
29. Davierwala, A. P. *et al.* The synthetic genetic interaction spectrum of essential genes. *Nat. Genet.* **37,** 1147–1152 (2005).
30. Opekarova, M., Caspari, T. & Tanner, W. Unidirectional arginine transport in reconstituted plasma-membrane vesicles from yeast overexpressing CAN1. *Eur. J. Biochem.* **211,** 683–688 (1993).
31. Rothbauer, U. *et al.* Targeting and tracing antigens in live cells with fluorescent nanobodies. *Nat. Methods* **3,** 887–889 (2006).
32. Walther, T. C. *et al.* Eisosomes mark static sites of endocytosis. *Nature* **439,** 998–1003 (2006).
33. Frohlich, F. *et al.* A genome-wide screen for genes affecting eisosomes reveals Nce102 function in sphingolipid signaling. *J. Cell Biol.* **185,** 1227–1242 (2009).
34. Engelman, D. M. Membranes are more mosaic than fluid. *Nature* **438,** 578–580 (2005).
35. Ejsing, C. S. *et al.* Global analysis of the yeast lipidome by quantitative shotgun mass spectrometry. *Proc. Natl Acad. Sci. USA* **106,** 2136–2141 (2009).
36. Sharpe, H. J., Stevens, T. J. & Munro, S. A comprehensive comparison of transmembrane domains reveals organelle-specific properties. *Cell* **142,** 158–169 (2010).
37. Gallego, O. *et al.* A systematic screen for protein–lipid interactions in *Saccharomyces cerevisiae*. *Mol. Syst. Biol.* **6,** 430 (2010).
38. Hite, R. K., Li, Z. & Walz, T. Principles of membrane protein interactions with annular lipids deduced from aquaporin-0 2D crystals. *EMBO J.* **29,** 1652–1658 (2010).
39. Lehtonen, J. Y., Holopainen, J. M. & Kinnunen, P. K. Evidence for the formation of microdomains in liquid crystalline large unilamellar vesicles caused by hydrophobic mismatch of the constituent phospholipids. *Biophys. J.* **70,** 1753–1760 (1996).
40. Thomas, C. L., Bayer, E. M., Ritzenthaler, C., Fernandez-Calvino, L. & Maule, A. J. Specific targeting of a plasmodesmal protein affecting cell-to-cell communication. *PLoS Biol.* **6,** e7 (2008).
41. Day, C. A. & Kenworthy, A. K. Tracking microdomain dynamics in cell membranes. *Biochim. Biophys. Acta* **1788,** 245–253 (2009).
42. Fan, J., Sammalkorpi, M. & Haataja, M. Formation and regulation of lipid microdomains in cell membranes: theory, modeling, and speculation. *FEBS Lett.* **584,** 1678–1684 (2010).
43. Bagnat, M. & Simons, K. Cell surface polarization during yeast mating. *Proc. Natl Acad. Sci. USA* **99,** 14183–14188 (2002).
44. Tyteca, D. *et al.* Three unrelated sphingomyelin analogs spontaneously cluster into plasma membrane micrometric domains. *Biochim. Biophys. Acta* **1798,** 909–927 (2010).
45. Lauwers, E. & André, B. Association of yeast transporters with detergent-resistant membranes correlates with their cell-surface location. *Traffic* **7,** 1045–1059 (2006).
46. Opekarova, M., Malinska, K., Novakova, L. & Tanner, W. Differential effect of phosphatidylethanolamine depletion on raft proteins: further evidence for diversity of rafts in *Saccharomyces cerevisiae*. *Biochim. Biophys. Acta* **1711,** 87–95 (2005).

METHODS

Plasma-membrane proteome. A set of 279 proteins associated with the plasma membrane in *S. cerevisiae* was manually classified with respect to biological function and type of membrane anchor (Supplementary Table S1). We further selected 46 proteins covering all major functional categories (Fig. 1a). Protein sequences were obtained from Uniprot V.18.may2010. TMSs were identified using a consensus prediction tool. We implemented Java packages to read MetaTM predictions for all plasma-membrane proteins from the Java DAS client library (Dasobert, www.spice-3d.org/dasobert). Information on lipid anchors was obtained from Uniprot and online prediction tools. Protein expression values for tandem affinity purification (TAP)-tagged proteins were obtained from ref. 17. Only proteins with available expression data were included in the comparison with cortical GFP levels (Fig. 2f).

Plasmids and strains. Plasmids pRS315 and pRS316 were used for carboxy-terminal tagging. Primers for the TMSs of Pmp1, Fet3 and Mid2 were directly ligated into vectors. The FetPmp chimaera was generated using recombination cloning in yeast. Ras2 was cloned into a pRS306-derived vector containing amino-terminal GFP. All constructs were verified by sequencing. Genomic tagging was performed as described previously[47]. Plasmids and strains are listed in Supplementary Tables S7 and S8.

Yeast growth conditions. All stains were based on *S. cerevisiae* strain BY4741 (Euroscarf). Unless otherwise indicated, strains from the UCSF GFP collection[48] were used. Cells were grown in synthetic media at 30 °C to an attenuance (D) of 0.2–0.6 at 600 nm. Hxt2–GFP- and Hxt6–GFP-expressing cells were grown with 0.5% glucose, Bio5–GFP-expressing cells without biotin and Gap1–GFP-expressing cells in minimal medium. *mss4-102* cells were grown at 37 °C for 30 min and imaged at the restrictive temperature. ACP–Sag1-expressing cells were grown overnight and diluted to $D_{600\,nm} = 0.1$ in YP 2% raffinose. Protein expression was induced for 4 h in 2% galactose. After washing twice in labelling buffer (50 mM Tris–HCl at pH 8.8, 100 mM NaCl and 10 mM $MgCl_2$), labelling was performed for 20 min at 30 °C in the dark with 5 µM ATTO488–CoA and 1 µM ACP synthase (NEB). The reaction was stopped by washing twice with labelling buffer.

Latrunculin B was used at 200 µM. For cell wall digestion, 5 µl 100T Zymolyase was added to 100 µl cell suspension. Myriocin (Sigma) was added at 5 µM for 1 h. Δ*cho1* strains were grown on media supplemented with 1 mM choline. For rescue experiments, lyso-phosphatidylserine (Avanti) was added at 20 µg ml^{-1} for the indicated time. Canavanine growth assays were performed on arginine-free media containing 5 µg ml^{-1} canavanine. The iron-depletion growth assay was performed in synthetic medium containing 10 µg ml^{-1} bathophenanthroline disulphonate (Alfa Aesar). $D_{600\,nm}$ was measured every 15 min in a Bioscreen C shaker (Oy Growth Curves Ab).

TIRFM. Images were acquired on an iMIC stand (Till Photonics) with an Olympus ×100 1.45 NA objective. DPSS lasers (75 mW) at 488 nm (Coherent Sapphire) and 561 nm (Cobolt Jive) were selected through an acousto-optical tunable filter. A two-axis scan head was used to adjust incidence angles or FRAP position. An additional galvanometer was used to switch between illumination paths. Images were collected with an Andor iXON DU-897 EMCCD camera controlled by the Live Acquisition (Till Photonics) software. For two-colour TIRFM, incidence angles were adjusted for each laser. Separate filters were used for detection of green and red fluorophores. Fluorescent beads (Invitrogen) were mixed with samples to correct for offset between filters. Living yeast cells labelled with ATTO488 at the extracellular domain of Sag1 were imaged as described previously[49]. Coverslips were cleaned with 1 M NaOH overnight, washed twice with double-distilled H_2O and stored in pure ethanol. To immobilize cells, coverslips were pre-coated with 2 mg ml^{-1} concanavalin A (Sigma).

TIRF-SIM. TIRF-SIM was performed on a custom-made set-up based on an inverted microscope (Leica DM-IRBE) according to ref. 13. A 488 nm argon-ion laser (2214-20SL, JDSU) beam was guided through an acousto-optical tunable filter (Pegasus Optik), expanded by a 20× beam expander (SILL Optics) and reflected by a spatial light modulator (LCR-2500, Holoeye Photonics). Computer-generated phase gratings diffracted the beam into the ±1 diffraction orders. A polarization filter and a motorized half-wave plate ensured a high degree of linear s-polarization. A lens doublet focused the beams and an aperture mask blocked unwanted diffraction orders. The remaining first diffraction orders were guided by a 4f lens system to opposite positions in the total internal reflection region of the back focal plane of the objective (HCX PL APO, 1.46 NA ×100, Leica). The two emanating beams created an evanescent wave with a sinusoidal excitation pattern. Fluorescent light was selected with a dichroic mirror (Chroma) and a 550/88 emission filter (Semrock). Modulated fluorescence images were recorded by a CCD (charge-coupled device) camera (Hamamatsu C8484-05G). For one super-resolved image, nine raw images were acquired, corresponding to three grating orientations (0°, 60° and 120°) with three phases (0°, 120° and 240°) each, all shown as phase holograms on the spatial light modulator. For reconstructions of the final images from the raw data, a MATLAB-based algorithm provided by R. Heintzmann (University of Jena, Germany) was used[50].

Image processing. TIRFM images were deconvolved using the classical maximum likelihood estimation algorithm in Huygens Professional 3.4 (Scientific Volume Imaging B.V.). Point spread functions were measured from >20 green/red fluorescent latex beads imaged separately for each channel and experimental setting. For visualization purposes, images were projected to 300 dpi in all figures. Analysis and quantifications were performed on non-projected deconvolved images.

FRAP and autocorrelation. For FRAP experiments, a single spot was bleached and recovery was fitted with a simple exponential fit $y = a(1 - e^{(-xb)})$. Half-times $t_{1/2} = -\log(0.5)/b$ and mobile fractions ($Mf = a$) were calculated for FRAP experiments that could be reliably fitted. Recoveries of rapidly diffusing proteins were recorded for 15 s. All other proteins were observed for 5 min. FRAP evaluations were carried out with Matlab. Five frames were used as a reference before bleaching. A position in the same cell but distant from the FRAP spot was used as a bleaching control. For image autocorrelation analyses, pixel intensities I within a region on the cell surface were correlated over time. We calculated the Pearson correlation coefficient ρ by comparing intensities at each time point ($t = i$) with those in the first frame ($t = 0$), thus evaluating the variation between intensity values $\rho(I_{t=0}, I_{t=i})$.

Co-localization pipeline. Data analysis was automated to avoid bias. First, cells were detected and extracted from images: maximum projections of red and green channels were blurred (Gaussian) and filtered (median) to smooth out spatial patterns to the cell boundaries. Cells were then detected by searching for high-intensity peaks and detecting the cell boundaries by derivations in x and y directions. Second, extracted cell images were separately deconvolved in each channel. Third, beads that were mixed with cells before imaging were deconvolved and used to determine the x–y shift of the two filter sets for each image. Finally, after correcting the filter shift with subpixel resolution, co-localization was quantified using a linear overlap coefficient (see below). All algorithms and evaluations were implemented in Java and Matlab.

Co-localization coefficient. Co-localization between proteins was quantified using a squared Manders overlap coefficient[22] with $M = (\Sigma R_i G_i)^2 / \Sigma R_i^2 \Sigma G_i^2$. Thresholding procedures were not reproducible enough to quantify variable network-like patterns, but contrast after deconvolution was sufficiently high to allow reproducible co-localization measurements without thresholding. To minimize contributions from background fluorescence, regions of interest were selected within cells. Intensity values in each channel were scaled to the full 8-bit range. A Java package was implemented (using the ImageJ Application Programming Interface (API) rsbweb.nih.gov/ij and classes from www.uhnres.utoronto.ca/facilities/wcif) to quantify co-localization. We evaluated the performance of the Manders overlap with synthetic images (Supplementary Fig. S3b–d) and defined a linear co-localization coefficient by using the squared Manders overlap (referred to as the overlap coefficient throughout our study). To obtain decoy overlap values, red and green channels were shuffled between cells from a particular strain (Fig. 5a,b) or between cells with a particular intensity distribution (Fig. 5d).

Sequence similarity of TMSs. Similarities of TMSs were calculated by pair-wise global alignments with a Java implementation of the Needlemann–Wunsch algorithm. The JAligner API (jaligner.sourceforge.net) for local alignments was adjusted to calculate global alignments using Meta-CLustering Algorithm (MCLA) matrices of chemical similarity (gap open = 5, gap extend = 0.5). TMS similarities were determined from pair-wise alignments. To determine sequence similarities between randomly generated TMSs, we shuffled amino acids across all TMSs while preserving TMS length and calculated all-against-all pair-wise alignments for the decoy TMS set. The median random similarity was 43% (interquartile range: 38–48%). Therefore, 46% similarity between the TMSs of Fet3 and Pmp1 was considered random.

Abundance and intensity distributions of plasma-membrane proteins. Cells were grown overnight in a 96-well plate, diluted and transferred to eight-well glass-bottom slides (ibidi). z stacks were taken for >50 cells per strain. Intensities along equators were normalized and quantified in Matlab. Intensity distribution was

DOI: 10.1038/ncb2487

defined as the area above normalized, cumulative intensity histograms of TIRFM images. Joint abundance or intensity distribution of two proteins was calculated by summing their individual values.

Statistical analysis. Statistical analyses were performed in R (V. 2.8.1, www.r-project.org). For comparison of conditions, we applied two-sided two-sample t-tests ($\alpha = 0.05$) with Bonferroni correction.

Data are shown as mean ± s.e.m or box plots. Median, upper and lower quartiles of data distributions are indicated as the box; solid lines indicate the 95% confidence interval. Outliers are marked with circles. z scores were calculated to indicate divergence of decoy intensity distributions (Fig. 5d). A divergence of 1 standard deviation (σ, Supplementary Fig. S7c) corresponds to a z score of 0.065. Pearson correlation coefficients (R) and the significance of correlation (P) were determined for scattered data sets.

47. Janke, C. *et al*. A versatile toolbox for PCR-based tagging of yeast genes: new fluorescent proteins, more markers and promoter substitution cassettes. *Yeast* **21,** 947–962 (2004).
48. Huh, W-K. *et al*. Global analysis of protein localization in budding yeast. *Nature* **425,** 686–691 (2003).
49. George, N., Pick, H., Vogel, H., Johnsson, N. & Johnsson, K. Specific labeling of cell surface proteins with chemically diverse compounds. *J. Am. Chem. Soc.* **126,** 8896–8897 (2004).
50. Hirvonen, L. M., Wicker, K., Mandula, O. & Heintzmann, R. Structured illumination microscopy of a living cell. *Eur. Biophys. J.* **38,** 807–812 (2009).

Correction notice

Nature Cell Biology **14,** 640-648 (2012) | doi: 10.1038/ncb2487

Patchwork organization of the yeast plasma membrane into numerous coexisting domains

Felix Spira, Nikola S. Mueller, Gisela Beck, Philipp von Olshausen, Joachim Beig & Roland Wedlich-Söldner

In the version of this Resource Article initially published online, the heading for the first column in Supplementary Table S5 was incorrect. The correct label for the column is “ProteinRFP–ProteinGFP”. This error has been corrected.

Correction notice

Nature Cell Biology **14**, 640-648 (2012) | doi: 10.1038/ncb2487

Patchwork organization of the yeast plasma membrane into numerous coexisting domains

Felix Spira, Nikola S. Mueller, Gisela Beck, Philipp von Olshausen, Joachim Beig & Roland Wedlich-Söldner

In the version of this Resource Article initially published online, the labels for panels a and b were reversed in the figure and legend for supplementary figure S5. Figure S5a shows Pma1RFP whereas figure S5b shows Sur7RFP. This error has been corrected.

DOI: 10.1038/ncb2487

nature cell biology

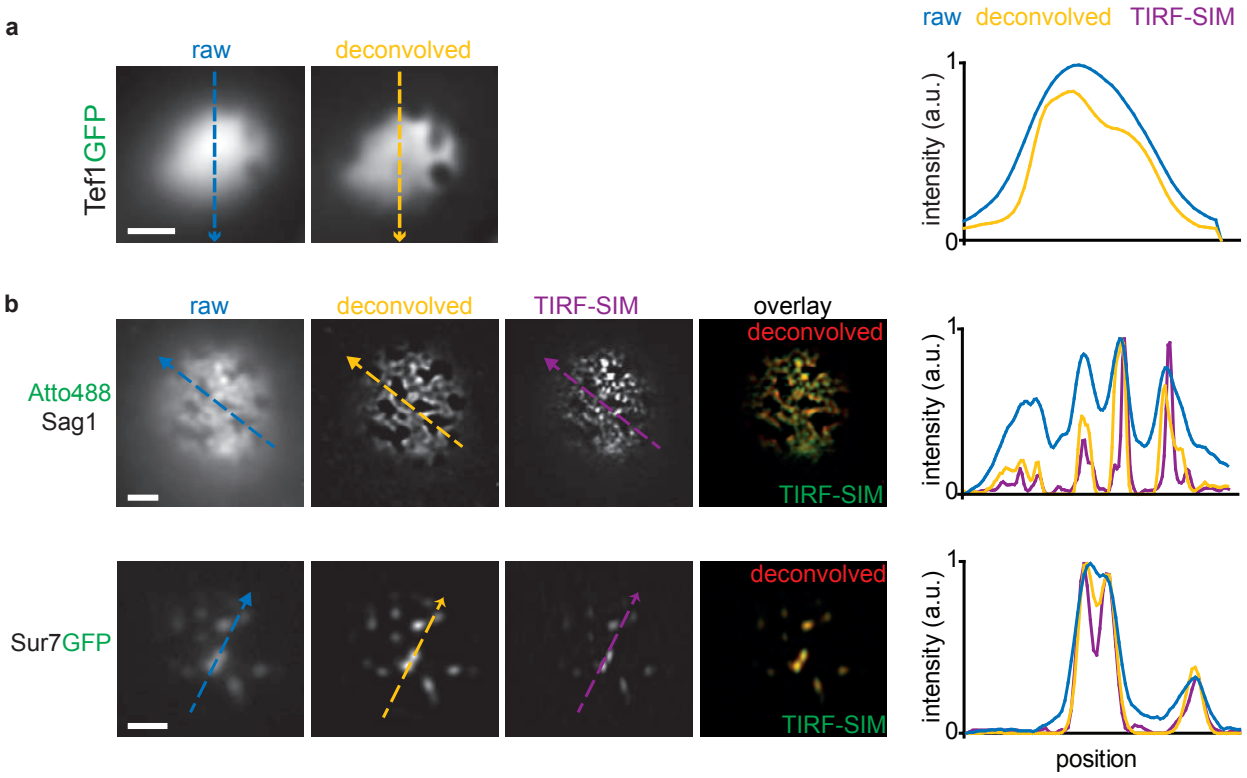

Figure S1 Deconvolution and superresolution imaging. **(a)** Raw and deconvolved TIRFM images of a cell expressing Tef1GFP. Intensity profiles are shown along the indicated dotted lines. Note that deconvolution generates no artefactual features and retains the homogeneous distribution visible in the raw TIRFM image. **(b)** Comparison of raw, deconvolved and TIRF-SIM images of Atto488-labeled Sag1 and Sur7GFP, respectively. Intensity profiles are shown along the indicated dotted lines. Deconvolution does not create novel features, but increases image contrast. The overlay shows that patch and network like patterns in deconvolved and TIRF-SIM images are very similar. Scale bars: 2 μm.

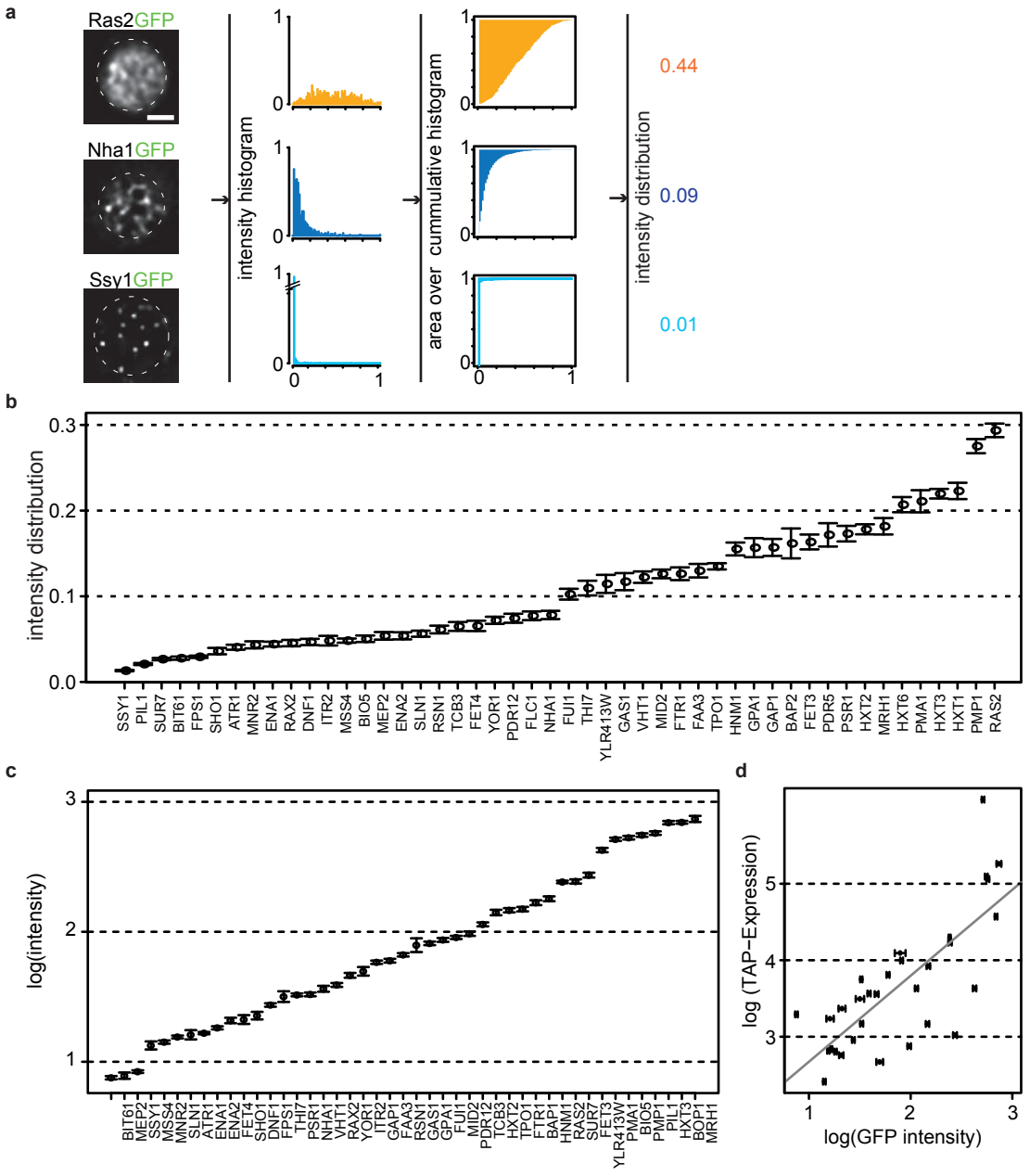

Figure S2 Intensity distribution and protein abundance. **(a)** To obtain intensity distributions, 64-bin intensity histograms were calculated from deconvolved images. Intensity distributions correspond to the area above cumulative histograms. **(b)** Distribution of intensity distributions for all proteins in the test set (Supplementary Table S3). **(c)** Abundance of peripheral GFP tagged proteins used in this study (Supplementary Table S4). **(d)** Correlation between protein levels obtained from a TAP expression screen with measured cortical GFP Signals. Scale bar: 2 µm.

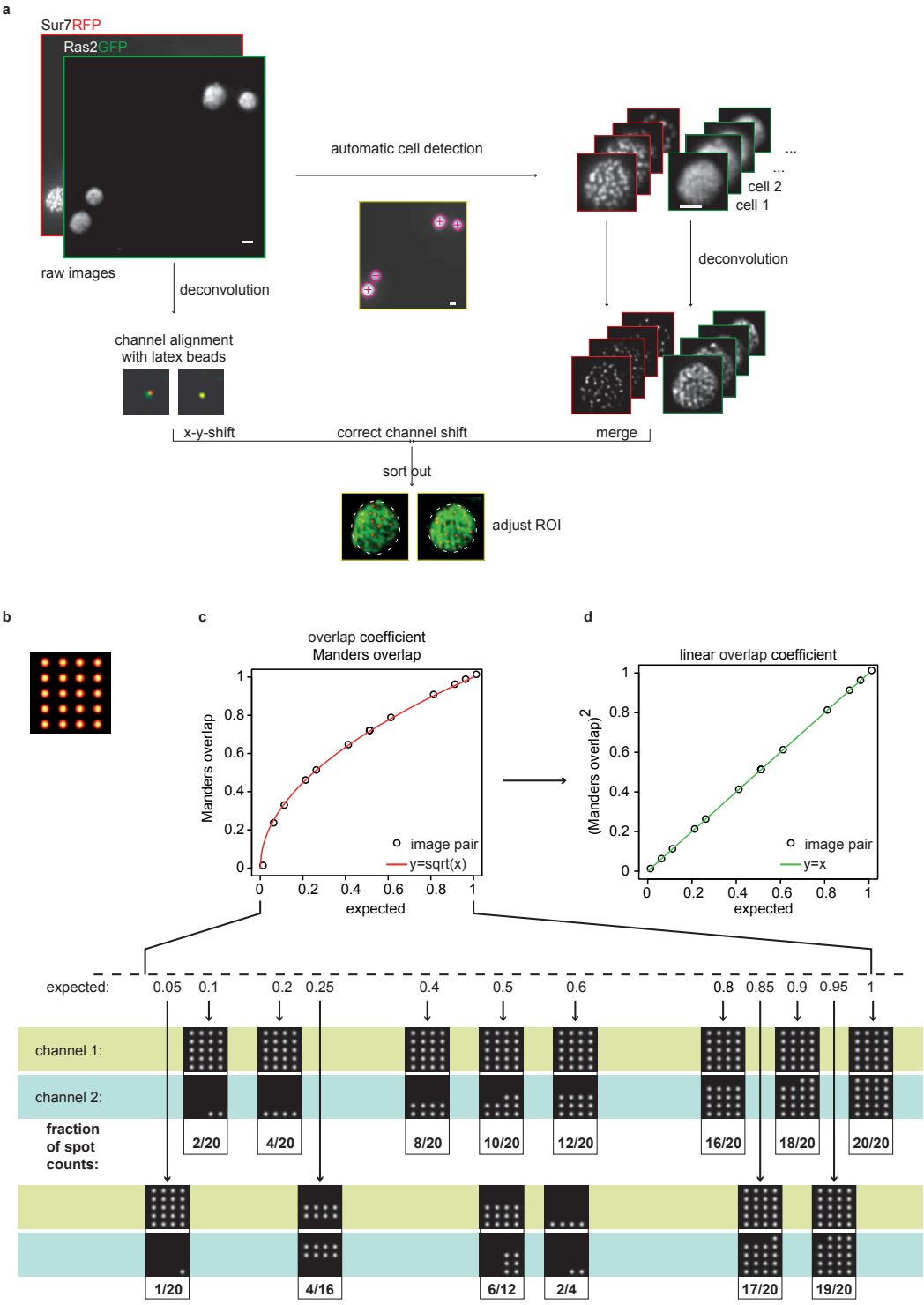

Figure S3 Workflow for colocalization screen. **(a)** Workflow used to process TIRFM image data prior to analysis is depicted (using Ras2GFP and Sur7RFP as examples). All steps following image acquisition, with the exception of manual selection of the region of interest (ROI) were automated. **(b)** Synthetic images were generated to mimic patch-like patterns. Individual dots were generated with Gaussian blur. **(c)** To evaluate colocalization values obtained with the classical Manders coefficient, results were benchmarked against synthetic images. Expected colocalization was defined as fraction of patches common to both channels. We found that the Manders overlap scaled as the square root of expected colocalization values (red fitted curve). **(d)** A linear colocalization coefficient was obtained by squaring the Manders overlap (green fitted curve). This squared colocalization coefficient was used throughout our study (= overlap coefficient).

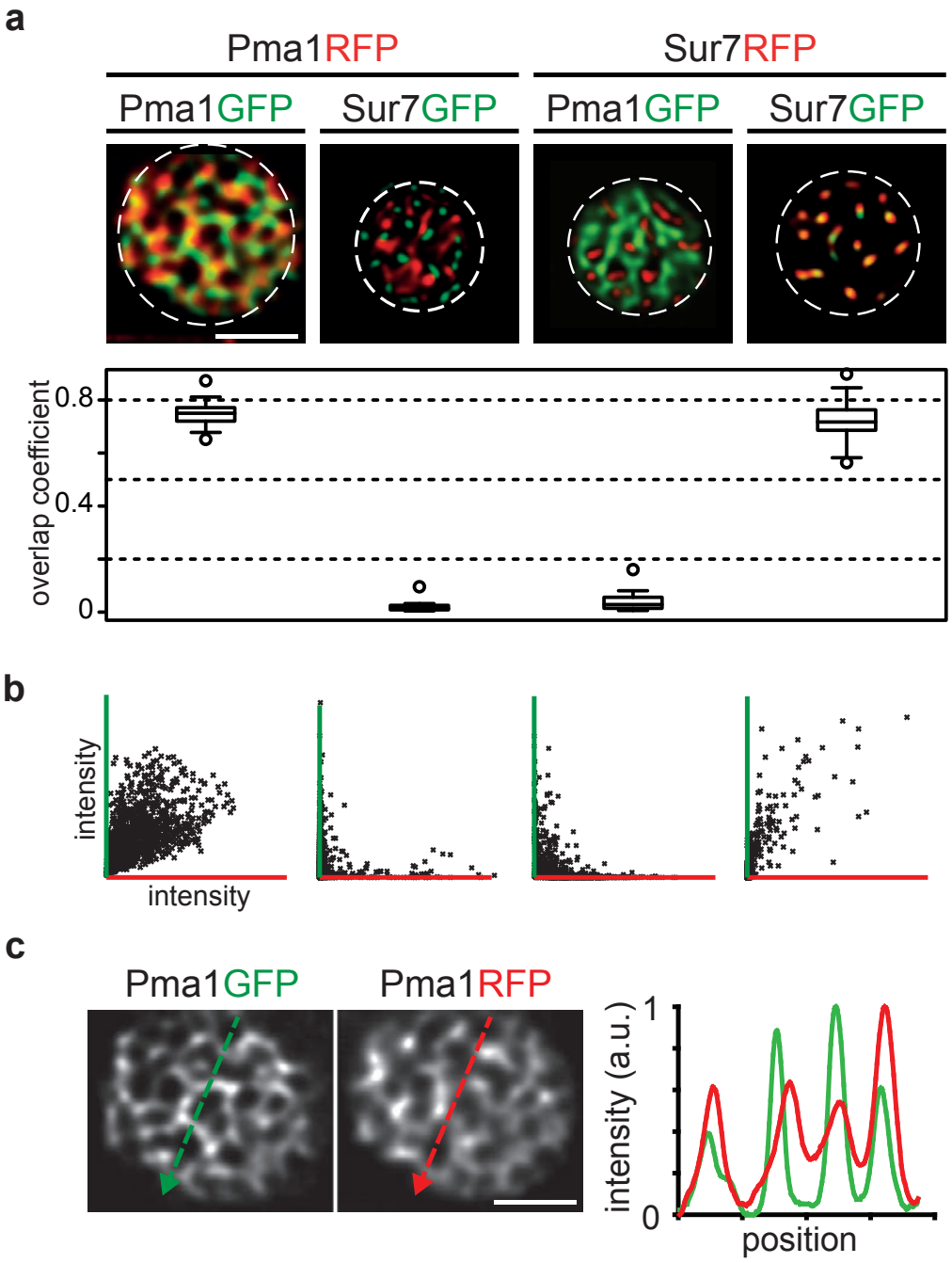

Figure S4 Colocalization controls. The linear colocalization coefficient was experimentally evaluated. Sur7 and Pma1 form non-overlapping domains, which was consistent with low overlap coefficients < 0.2. Overlap coefficients for identical proteins were > 0.7. **(a)** TIRFM images and Overlap coefficients. **(b)** Scatter plots of images shown in (a). **(c)** Individual channels of Pma1GFP and Pma1RFP linescan along the indicate line shows a nearly perfect colocalization of both channels. Scale bars: 2 μm.

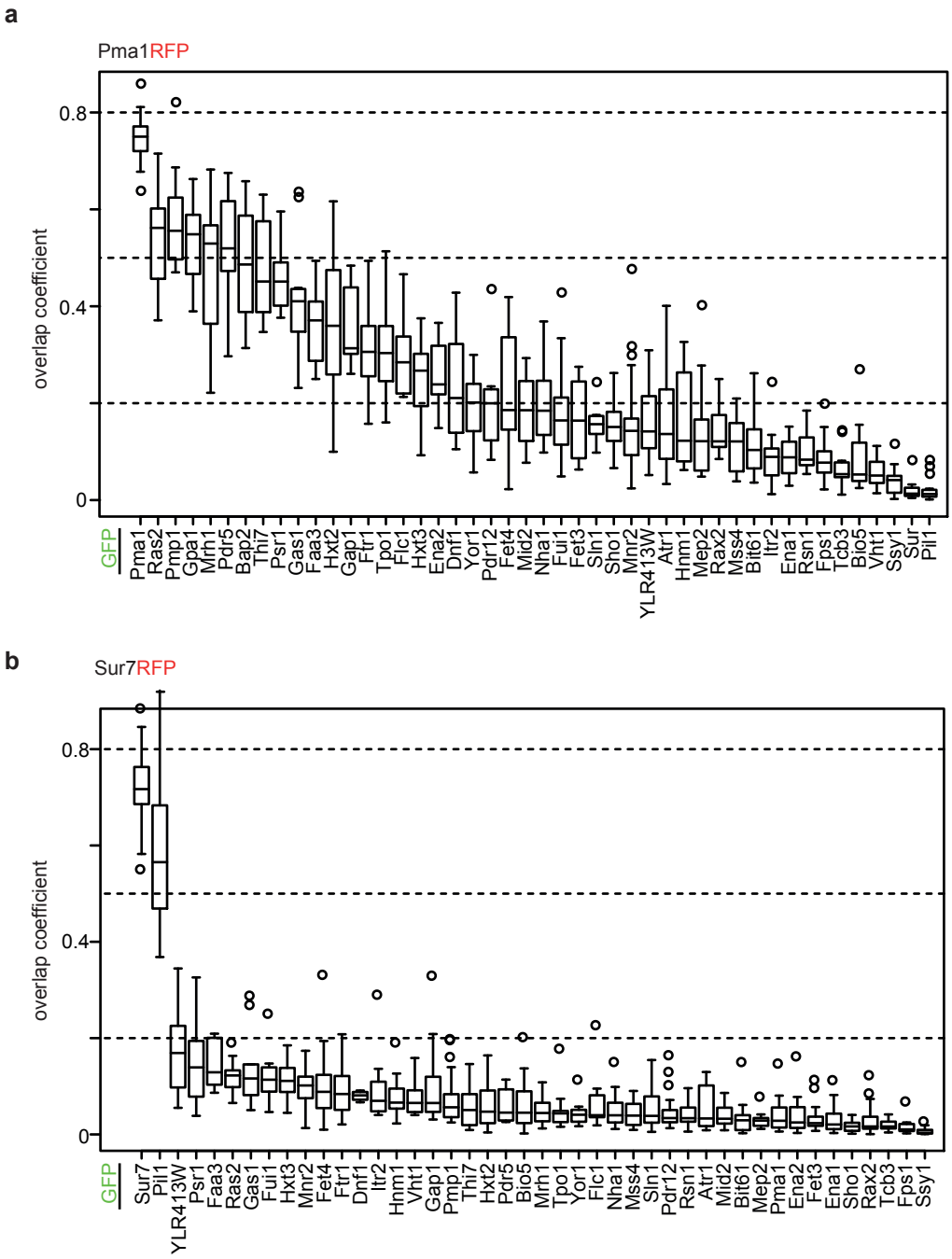

Figure S5 Colocalization of PM proteins with Sur7 and Pma1. Box plots of overlap coefficients for all 46 proteins tested with **(a)** Pma1RFP or **(b)** Sur7RFP.

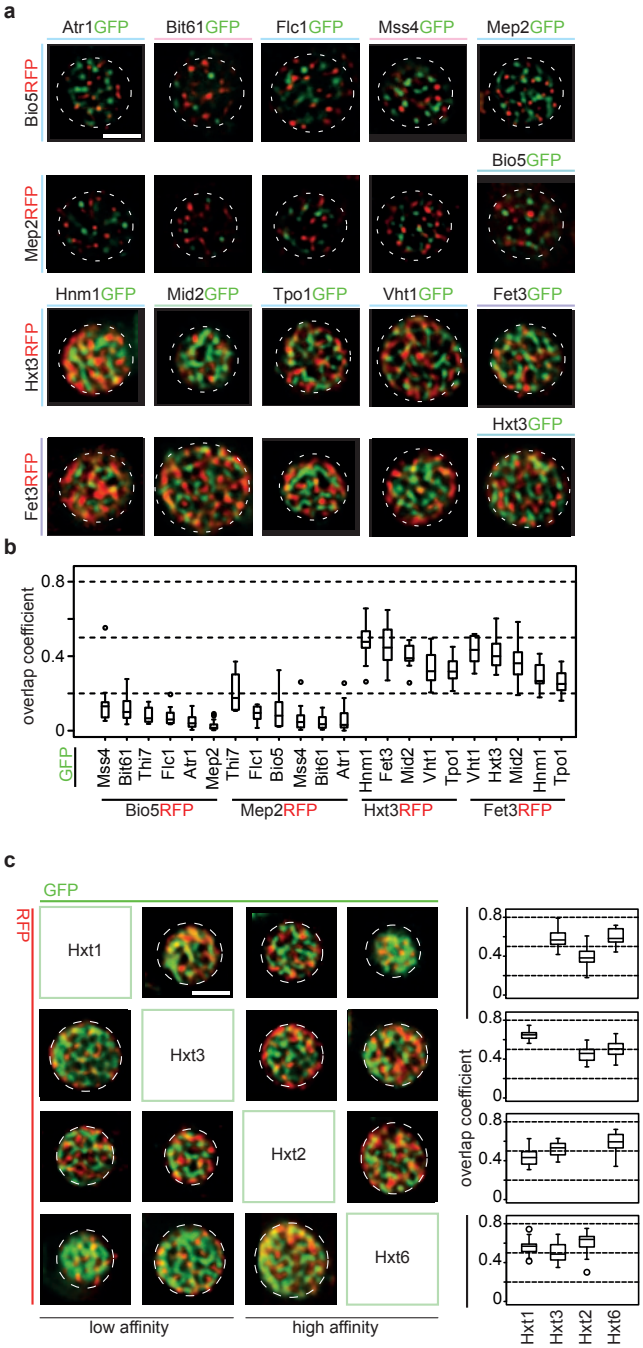

Figure S6 Colocalization of different proteins. **(a)** Patch-forming proteins Bio5RFP and Mep2RFP and network-forming proteins Hxt3RFP and Fet3RFP were colocalized against additional proteins. **(b)** Overlap coefficients for protein pairs indicated in (a). **(c)** All-against-all two-colour TIRFM images of low (Hxt1/3) and high (Hxt6/2) affinity hexose transporters. Boxplots show the distribution of overlap coefficients. Scale bars: 2μm.

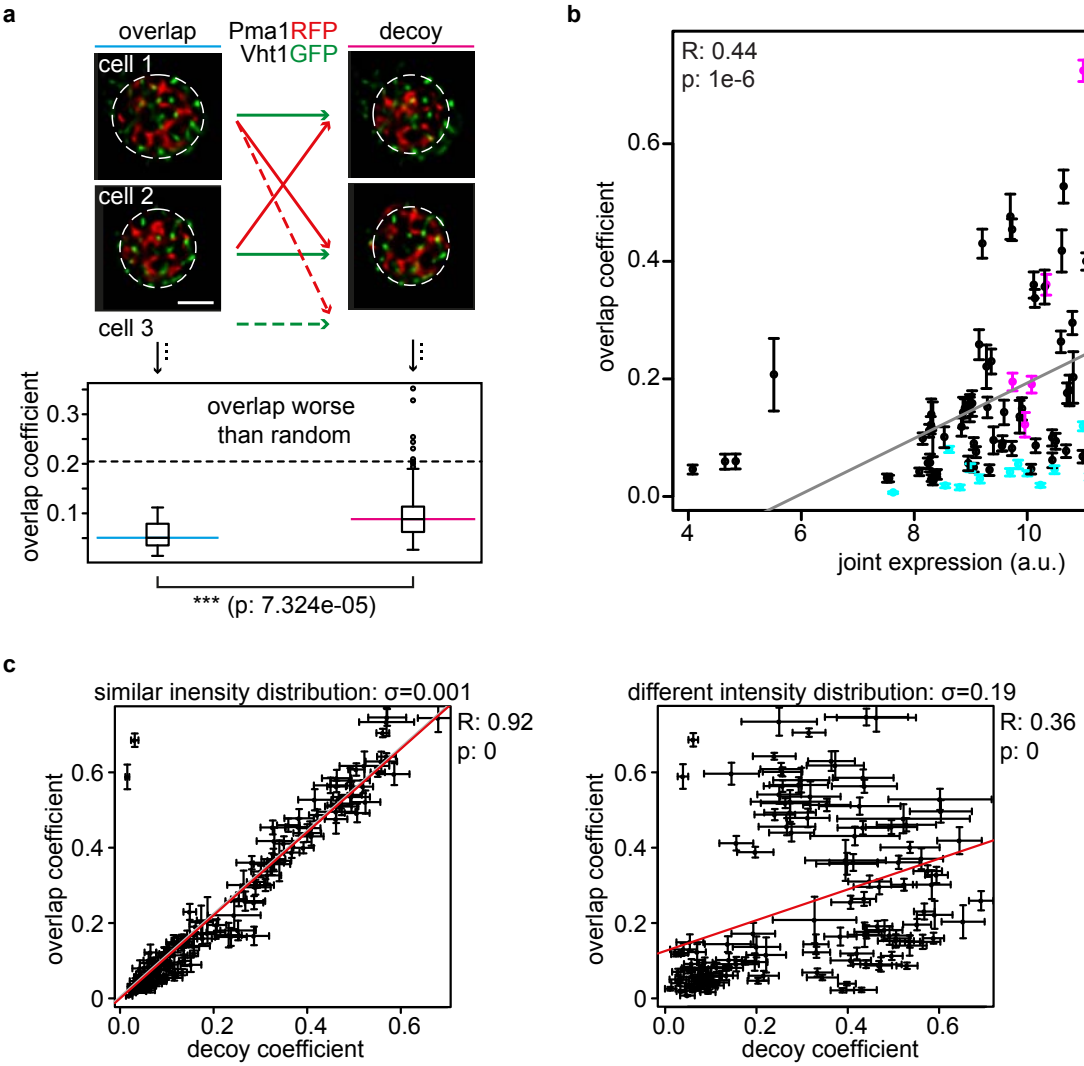

Figure S7 Statistical evaluation of overlap coefficients. **(a)** Pma1RFP and Vht1GFP colocalize less than expected from random overlap values. **(b)** Weak correlation of overlap coefficients and joint expression levels. **(c)** Correlation plots between decoy and real overlap coefficients for decoy values calculated from cells with similar or divergent intensity distributions. Divergence is indicated as σ. R and p values for correlations are shown. Scale bar: 2 μm.

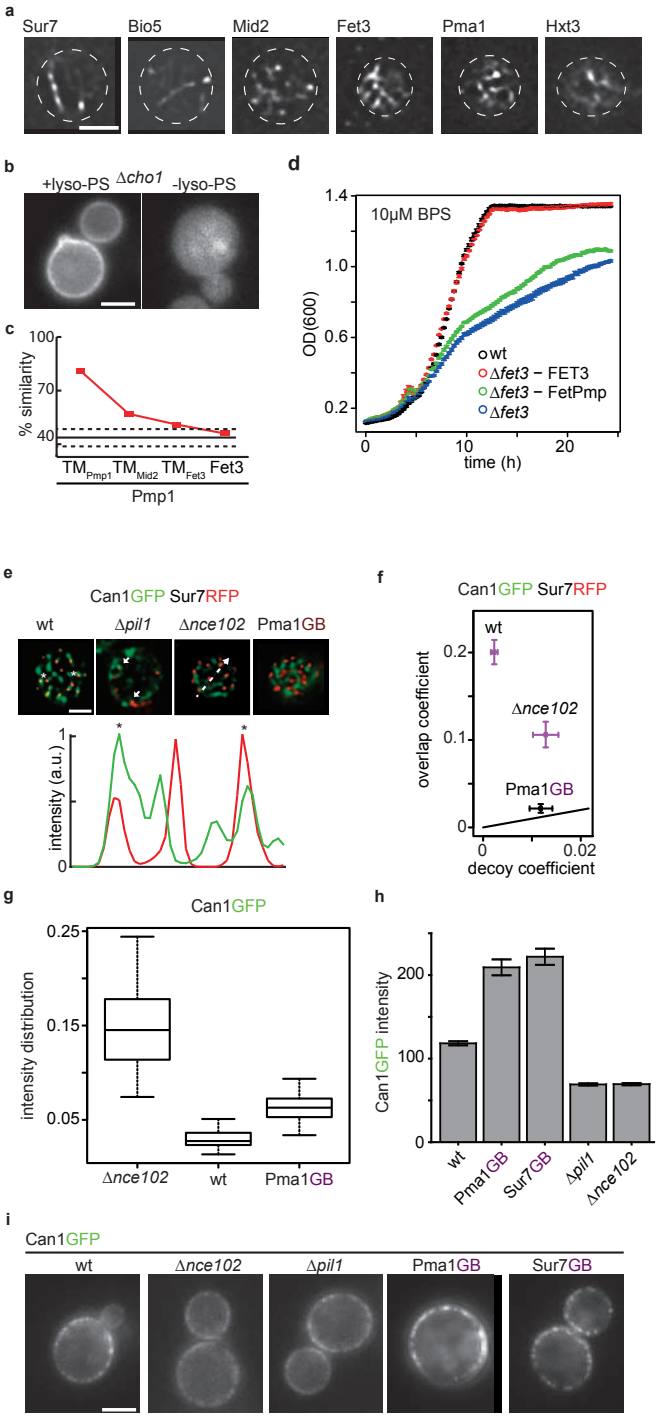

Figure S8 Perturbation of membrane patterns. **(a)** Cell wall degradation with Zymolyase induces aggregation of PM proteins. **(b)** GFPLactC2 is cytosolic in Δ*cho1* cells but is recruited to the PM after addition of lyso-PS for 1 h. **(c)** Plot of sequence similarities between TM constructs and Pmp1. Range of random similarity values, indicated as dotted lines. **(d)** Growth of Δ*fet3* cells in iron depleted medium. Strains expressing the chimeric FetPmp are not rescued and grow poorly. **(e)** TIRFM images of wt, *Δpil1*, *Δnce102,* Pma1GB cells expressing Can1GFP and Sur7RFP. Asterisk: Colocalization of Can1GFP and Sur7RFP. Arrowheads: Remnants with colocalizing Can1GFP and Sur7RFP. The line scan on the bottom was taken along the dotted arrow shown in the *Δnce102* image. Partial colocalization in intensity peaks is marked by asterisks. **(f)** Overlap and decoy coefficients for TIRFM images of wt, *Δnce102,* Pma1GB cells expressing Can1GFP and Sur7RFP. Data points are shown as mean ± s.e.m. in both directions. Can1GFP colocalized significantly better than random with Sur7 in wt ($p < 10^{-14}$) and *Δnce102* ($p < 10^{-5}$) strains (indicated in magenta) but only at random levels in strains expressing Pma1GB. Black line marks identical decoy and overlap coefficients indicating area of random colocalization. **(g)** Box plots of intensity distributions for Can1GFP in wt, *Δnce102* and Pma1GB cells. **(h)** Quantification of Can1GFP abundance as GFP intensity at cell periphery in wt, Pma1GB, Sur7GB, *Δpil1* and *Δnce102* cells. **(i)** Equatorial widefield images of wt, *Δpil1*, *Δnce102,* Pma1GB and Sur7GB strains expressing Can1GFP. Scale bars: 2 μm.

Supplementary Tables

Supplementary Table 1
List of manually curated yeast PM proteins.
Column 1: Functional group
Column 2: Functional subgroup
Column 3: Protein name
Column 4&5: No. TMS or type of lipid anchor
Supplementary Table 2
Test set of proteins used in this study.
Column 1: Protein name
Column 2: TIRFM images of GFP fusions. Scale bars 2 µm. Dotted white lines indicate cell edges.
Column 3: Measured protein abundance.
Column 4: Calculated intensity distribution.
Column 5: FRAP analysis. Representative images of equatorial cross sections are shown. Yellow arrowheads mark FRAP positions. Kymographs were generated along the white dotted arrows over 5 min or 1 min (indicated with *). Numbers of analysed cells are given in brackets next to kymographs.
Column 6: Recovery parameters. Where recovery could be fitted by single exponential curves, halftimes, mobile fractions and numbers of cells used for evaluation are given.
Column 7: Colocalization with Sur7RFP. Representative two colour TIRFM images are show. White dotted lines indicate cell rim. Scale bars 2 µm. Average colocalization coefficients ± s.e.m. are given with the number of cells measured (n).
Column 8: Same as column 6 but with Pma1RFP.
Column 9: Number of TMS. Lipid anchors are indicated by "l.a.".
Supplementary Table 3
Intensity distribution of proteins used in this study
Column 1: Protein name
Column 2: Intensity distribution
Column 3: s.e.m of intensity distribution
Column 4: Number of cells used for calculation of the intensity distribution
Supplementary Table 4
Protein abundance
Column 1: Protein name
Column 2: Normalized GFP signal on the membrane
Column 3: s.e.m of GFP signal
Column 4: Number of cells used for quantification
Supplementary Table 5
Colocalization results. Overlap coefficient for pairs analyzed in this study.
Column 1: Proteins fused to RFP and GFP
Column 2: Mean overlap coefficient
Column 3: s.e.m.
Column 4: Number of cells analyzed
Supplementary Table 6
Statistical analysis of colocalization
Column 1: Comparison of overlap and decoy coefficients
Column 2: Protein pair
Column 3: Colocalization value
Column 4: p-value
Supplementary Table 7
Plasmid list.
Column 1: Plasmid number
Column 2: Plasmid description
Column 3: Origin of plasmid
Supplementary Table 8
Strain list.
Column 1: Strain number
Column 2: Strain genotype
Supplementary Table 9
Factors influencing distribution patterns.
Column 1: Strains and conditions compared 8A-B).
Column 2: Significant change (* if $p<0.05$).
Column 3: p-value
Column 4: Mean intensity distribution for A.
Column 5: Number of images for A.
Column 6: Mean intensity distribution for B.
Column 7: Number of images for B.

Supplementary Movie Legends
Supplementary Movies 1-4
Time-lapse TIRFM movies of PM protein GFP fusions. Shown are (1) patch-forming proteins Bio5 and Sur7, (2) network-forming TM proteins Hxt3 and Pma1, as well as (3) lipid anchored proteins Gpa1 and Ras2. (4) Lipid binding domains Lact-C2-GFP and 2x(PH)-Plcδ-GFP. Time indicated in each frame.
Supplementary Movie 5
Double colour movie Fet3GFP and Pma1RFP. Time indicated in each frame.